NiNPs@rGO Nanocomposites as Heterogenous Catalysts for Thiocarboxylation Cross-Coupling Reactions

L. Lombardi[a]
R. Mazzaro[b,c]
M. Gazzano[d]
A. Kovtun[d]
V. Morandi[b,c]
G. Bertuzzi[a]
M.Bandini*[a]

[a] Dipartimento di Chimica "Giacomo Ciamician", Alma Mater Studiorum – Università di Bologna, via Selmi 2, Bologna, Italy.
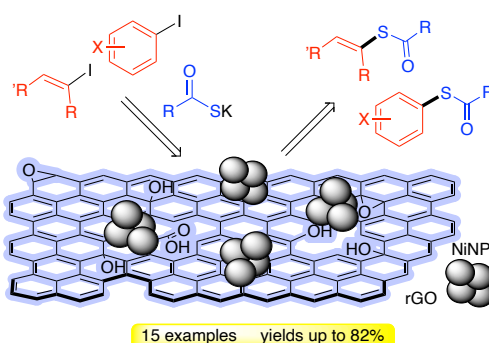
[b] CNR-IMM, Via Piero Gobetti 101, 40129 Bologna, Italy

[c] Dipartimento di Fisica e Astronomia "A. Righi", Alma Mater Studiorum – Università di Bologna, via Berti Pichat 6/2, Bologna, Italy

[d] Istituto per la Sintesi Organica e Fotoreattività (ISOF) – CNR, via Gobetti 101, 40129 Bologna.

marco.bandini@unibo.it

Click here to insert a dedication.

15 examples   yields up to 82%

Abstract A new type of ligand-free Ni-nanoparticles supported on rGO (size distribution average d = 9 ± 3 nm) is prepared and fully characterized via morphological (Fe-SEM), structural (P-XRD, HR-TEM) and spectroscopic (ICP-EOS, XPS) analysis tools. The metal composite was effectively employed in the unprecedented heterogeneously Ni-assisted cross-coupling reaction of aryl/vinyl iodides and thiocarboxylates. A range of sulphur-containing aryl as well as vinyl derivatives (15 examples) was achieved in high yields (up to 82%), mild reaction conditions and wide functional group tolerance.

Key words Heterogeneous catalysis; Ni-nanoparticles; Cross-coupling; Graphene oxide; Thiocarboxylation

Introduction

Transition metal catalyzed cross-coupling reactions are playing a prominent role in the synthesis of added value organic compounds. Starting from the "discovery phase" mainly focused on copper mediated processes and followed by the "1st wave discoveries" related to nickel catalysis, the past four decades have been dominated by the advent of Pd-mediated reactions commonly referred as the "2nd wave".[1]

In this realm, nickel catalysis is facing a renaissance by combining its unique adaptivity to redox protocols with a desirable functional group tolerance.[2] Although [Ni(II)] mediated cross-coupling strategies have been extensively and effectively exploited in organic synthesis,[2] the employment of highly reactive [Ni(0)] species as pre-catalysts is still suffering from concrete utilization in large scale manifolds due to the highly moisture-sensitive [Ni(0)] derivatives.

In this direction, the support of [Ni(0)] nanoparticles (NPs) onto inert matrix is commonly considered as a valuable tool to access easy-to-handle [Ni(0)] entities.[3] Supported [Ni(0)]-NPs already

found promising partnerships in C-C bond forming organic cross-coupling reactions (*i.e.* Heck, Suzuki-Miyaura, Sonogashira, Kumada-Corriu, P-arylations and direct C-H activations).[4] On the contrary the formation of C-hetero-connections[5] and more specifically C-S bonds has faced far less success also due to the well-known detrimental action of sulphur-compounds towards soft-transition metal catalysis.[6]

However, the large diffusion of Csp^2-S interconnections in natural occurring compounds[7] and in functional organic materials is tracing new trajectories in the development of environmentally benign heterogeneously catalyzed C-S cross-coupling reactions.[8]
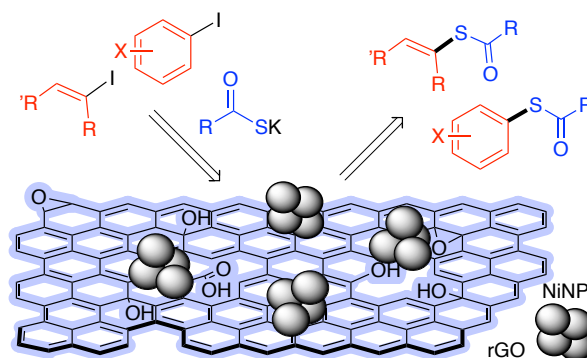
Figure 1. Graphical sketch of the present C-S bond forming cross-coupling reaction mediated by NiNPs@rGO.

In continuation with our ongoing interests in graphene oxide (GO) mediated organic transformations,[9] we herein focus on the realization of a ligand-free reduced graphene oxide- (rGO) supported Ni(0) nanocomposite[10] for the realization of a still underdeveloped methodology in the metal-catalyzed cross-coupling area: the Csp^2-S bond-forming protocols.[11,12] In particular, we envisioned that the nucleation activity of the oxygenated functional groups present in the rGO towards metal

nanoparticles, combined with a dedicated modulation of NP growth/dispersion, could provide a suitable platform for the realization of a catalytically active Ni(0)-based heterogeneous promoter for challenging cross-coupling reactions (Figure 1).

In this context, it is worth mentioning that, Ni nanoparticles dispersed on rGO nanosheets have already found found already applications in C-C bond forming cross-coupling protocols. Among the few, an elegant Sonogashira methodology was documented by means of magnetic nanoforms of Ni(0) (average size ~27 nm) that proved efficient in coupling aryl-iodides/bromides and terminal alkynes with a satisfying recoverability up to 6 runs.[4b] Homocoupling of alkynes (i.e. Glaser-Hay coupling) was also effectively carried out in the presence of magnetically active Ni-nanoparticles on reduced graphene oxide. The reusability profile displayed by the nickel-nanocomposite, and high range of functional group tolerance characterized the methodology.[4l] NiNPs were also effectively employed in an heterogeneously catalysed Kumada-Corriu reaction under mild conditions (i.e. rt, [Ni(0)]: 40 wt%). Notably, up to 6 consecutive runs were carried out by employing the same batch of catalyst and the contaminations by Mg(II) on the recovered Ni-composite did not affect its catalytic performance.[4a]

In the present study, we document on the synthesis and full characterization of two types of reduced graphene oxide/nickel nanocomposites **NiNP@rGO**, showing unique catalytic performance and narrow structure/activity correlation in the arylation/vinylation of potassium thiocarboxylates via C-S cross coupling.[12,13]

Results and discussion

Synthesis of the NiNPs@rGO

At the outset of the study, two different synthetic approaches for the realization of nanostructured rGO stabilized NiNPs were attempted with the aim of investigating the role of the NPs size/composition on their catalytic performance. In particular, two batches of rGO-Ni nanocomposites (**NiNP@rGO Type 1** and **NiNP@rGO Type 2**) were obtained by employing commercially available GO and $NiCl_2·6H_2O$, that upon suspension in deionized water and ethylene glycol, were simultaneously reduced in the presence of hydrazine hydrate[10a] or $NaBH_4$ (Scheme 1).[10e] ICP-OES analysis documented a significantly different metal loading for **Type 1** and **Type 2** metal composites. In particular, while the protocol based on hydrazine as reducing agent delivered a **NiNP@rGO** nanocomposite featuring a 69 wt% metal loading, the use of $NaBH_4$ resulted in a supported nickel catalyst **Type 2** with a much lower metal content (18 wt%).
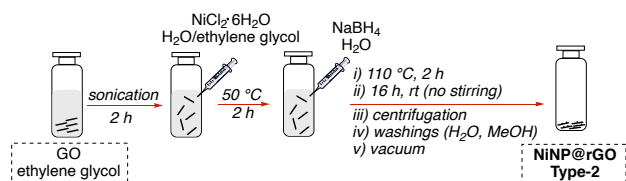
Scheme 1. Schematic representation of the synthetic sequence for the preparation of **NiNP@rGO Type 2** (see experimental section for details).

Bulk and film morphological characterization

Size, morphology, surface area and material polydispersity are crucial parameters that commonly concur to define the overall catalytic properties of NiNPs. Accordingly, full structural characterization of the Ni-rGO nanocomposites was performed. **NiNP@rGO NP Type 1** and **Type 2** were submitted to X-ray diffraction (XRD) investigation to get details on structural differences. The scans are presented in Figure 2. Pattern of **NiNP@rGO Type 1** is characterized by three sharp peaks owing to the cubic phase of crystalline nickel and by an asymmetric broad band with maximum at 23.9° (interlayer distance d = 0.372 nm), probably due to the overlap of several peaks deriving from GO portions reduced at different stages. Indeed, the peak of pristine GO is at 10.5° (d = 0.839 nm) and progressive reduction will shift it towards the position of the main graphite peak at 26.5° (d = 0.335 nm). Scan of **NiNP@rGO Type 2** shows several broad peaks: the main at 44.5° due to the overlap of 1 1 1 and 2 0 0 reflections of the cubic nickel phase, and the other one at 24.9° (d = 0.357 nm) due to reduced GO. Nickel particles are quite different in the two samples. Since an inverse relationship exists between peak width and size of crystallite domains (crystal size, C.S.), **Type 1** sample is characterized by C.S. of nickel domains equal to 21±2 nm, while it reduces to about 1.2 ± 0.3 nm in **Type 2** sample. The peak, or more properly in this case, the band of reduced GO is narrower, more symmetric and closer to graphite position in **Type 2** sample. A small amount of oxidized nickel seems to be present, too.
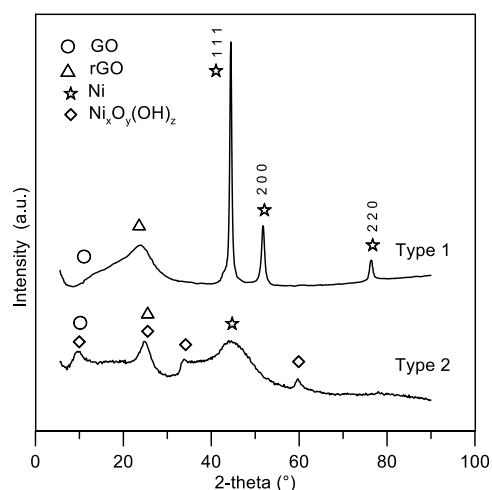
Figure 2. XRD patterns of **NiNP Type 1** and **NiNP Type 2** samples. Miller indexes for cubic nickel phase are reported.

The nanoscale structure and composition of the nanocomposite was thoroughly assessed by electron microscopy techniques. Figure 3a and 3d display the FE-SEM micrographs of **NiNP@rGO-Types 1** and **2**, highlighting a deep structural change induced by the different synthetic approach. **NiNP@rGO Type 1** composite is characterized by large spherical nanoparticles with an average size equal to 96 ± 36 nm, whose morphology is often embedded in a material fully covering their surface. On the other hand, **NiNP@rGO Type 2** composite displays much smaller nanoparticles (d = 9 ± 3 nm) decorating a clean substrate. Low

magnification HR-TEM micrographs of the same samples highlight the size difference between nanoparticles, as well as the nanostructured nature of the supporting substrate, displaying the typical wrinkles and folded edges of rGO (Figure 3b and 3e). By focusing on the rGO substrate (Figure S1), the material displays the typical features of a crystalline graphene-like structure. However, as often observed for rGO[14] and exfoliated graphene,[14] the number of layers is quite dishomogeneous, ranging between 1 and 20, due to the re-stacking of rGO flakes during the reduction process, as also observed in XRD. **NiNP@rGO Type 1** exhibits crystalline features (Figure 3c), with a d-spacing compatible to metallic Ni. In addition, diffraction fringes were observed on the edge of the nanoparticle, with a d-
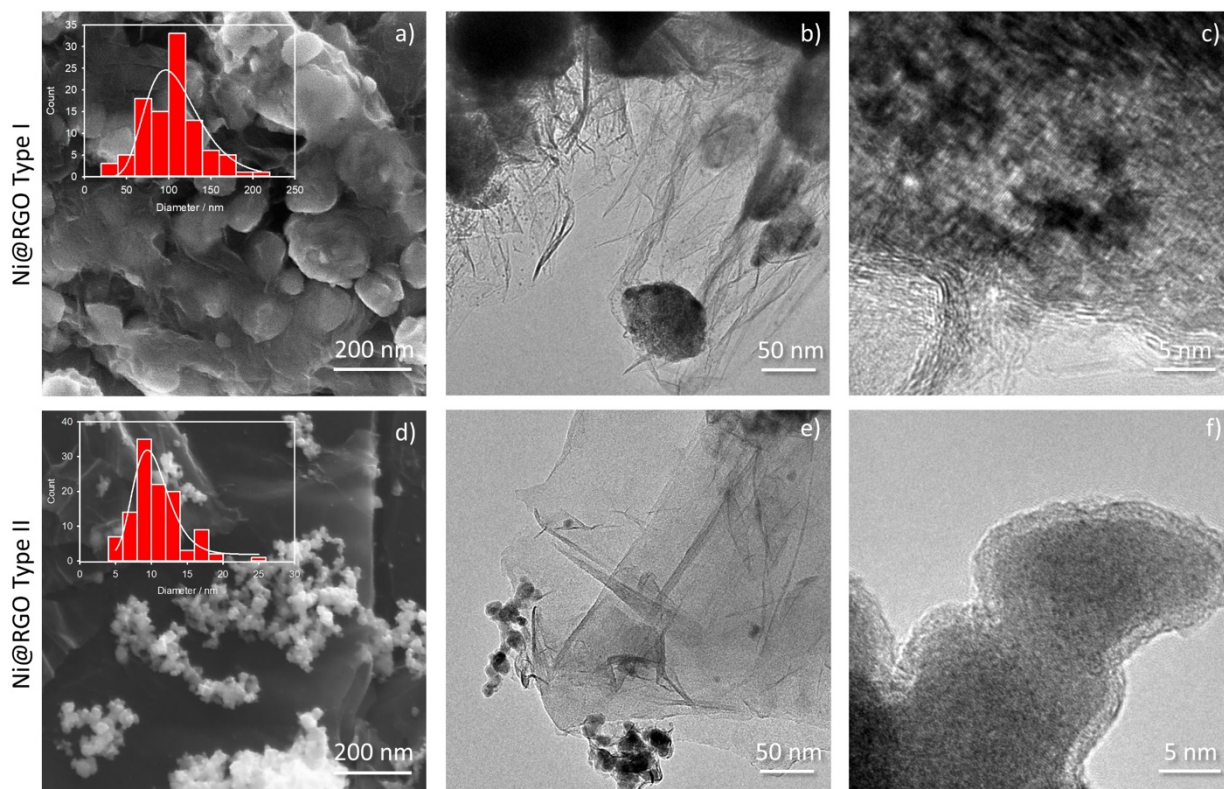

Figure 3. a) FE-SEM, b) Low magnification and c) High magnification HR-TEM micrographs of **NiNP@rGO Type 1**. In the inset, the size distribution histogram measured from FE-SEM micrograph and fitted with Log-Normal function. Figure d,e,f) display **NiNP@rGO Type 2** counterparts.

spacing close to 3.4 Å, matching the one of graphite (0,0,2) lattice planes. This suggests that a layer of rGO is fully wrapping the Ni nanoparticles in a tight-close structure. On the contrary, the **NiNP@rGO Type 2** did not display any crystal structure, probably due to the milder reduction technique employed. The nanoparticles are not wrapped in the rGO matrix, allowing their surface for higher availability towards the catalytic reaction. However, a thin (< 2 nm) amorphous layer with lower contrast covering the nanoparticles can be noticed on the HR-TEM micrograph (Figure 3f). The nature of this shell is hardly understood by HR-TEM due to the lack of crystalline features. However, EDS analysis displays a slight enhancement of the O/Ni ratio on the edge of the nanoparticle (Figure 4b), suggesting that a thin, partially oxidized layer is covering the nanoparticles. On the contrary, a slight increase in C-related signal is observed on the edge of a single NP in **Type 1** sample (Figure 4a). Moreover, no increment of O-related signal confirms the presence of the rGO coating. **NiNP@rGO Type 2** is also characterized by some isolated macro-aggregates of amorphous material exhibiting high nickel and boron content (Figure S2), resulting from the borohydride oxidation in presence of nickel salt.

Additionally, X-Ray Photoelectron Spectroscopy (XPS) was performed in order to understand the oxidation degree of both Ni nanoparticles and rGO support. Survey spectra of pristine GO and **NiNP@rGO Type 2** are reported in Figure 5a, while **NiNP@rGO Type 1** is reported in SI. Carbon, oxygen and nickel are present in both nanocomposites, but the oxidation degree has significant variations. From the fit of Ni 2p signal two chemical states can be discriminated: Ni(II), usually associated to Ni oxides or hydroxides, and the metallic Ni(0).[15] The surface amount of Ni in **NiNP@rGO Type 1** was relatively low (Table 1) and only Ni(II) was detected. On the contrary, both Ni(II) and Ni(0) species were found in higher quantity on the **NiNP@rGO Type 2** surface.

The low amount of Ni present in **NiNP@rGO Type 1** must not mislead: XPS is extremely surface sensitive (few nm) and when the Ni nanoparticles are wrapped in rGO, as showed in TEM images in Figure 3c, the XPS signal from Ni is significantly attenuated. Metallic phase was observed exclusively on **Type 2** in accordance with previous XPS results by Zhang,[16] where Ni clusters with core-shell structure were observed: the external

surface of the NP is composed by NiO and the inner core by metallic Ni. These results match the microscopy analysis.

Table 1. Relative amounts of Ni (in metallic and oxidised form) and O/C ratio at the surface of rGO support, as estimated by XPS data.

Sample	Ni(II) %[a]	Ni(0) %[a]	O/C[b]
GO	-	-	0.41±0.01
NiNP@rGO Type 1	0.23±0.05	-	0.13±0.01
NiNP@rGO Type 2	4.7 ±0.4	2.0±0.3	0.23±0.01

[a] Atomic concentration, values obtained from Ni 2p fit: Ni (II) 2p3/2 856.3 eV, Ni(0) 2p3/2 852.8 eV. [b] Oxygen to carbon ratio (O/C) was obtained from the fit of C 1s signal as described in ref. 18.

The chemical state of GO after reduction can be estimated by the deconvolution of C 1s signal. Unfortunately, the signal of oxygen (O 1s) has overlapping contributions from O atoms on rGO and O atoms on Ni oxides, while by using the fit of C 1s we can isolate only the C-O contributions.[17] GO is remarkably reduced in both cases, as showed in Table 1, nevertheless the two GO materials present some differences: the rGO obtained in **Type 2** procedure has a higher oxidation degree compared to **Type 1**, in agreement with the higher reduction efficiency of hydrazine hydrate with respect to NaBH₄. Summarizing, we observed a significant reduction of Ni and GO in **Type 2** as well, that was composed mainly by metallic Ni core and oxidized Ni shell nanoparticles supported on the aromatic domains (sp2 carbon) of rGO.
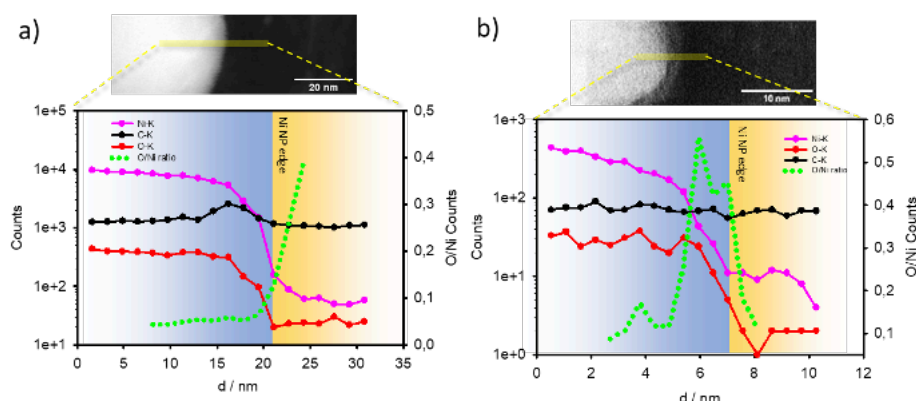
Figure 4. Ni, O and C K-α signals integrated from EDS spectra, extracted from the highlighted profile on the STEM-HAADF micrographs for **Type 1** a) and **Type 2** b) **NiNP@rGO** composites. The O/Ni signal ratio is also reported (green dotted line). The area relative to the **NiNP@rGO** is highlighted in light blue, while the supporting rGO area is highlighted in light yellow.
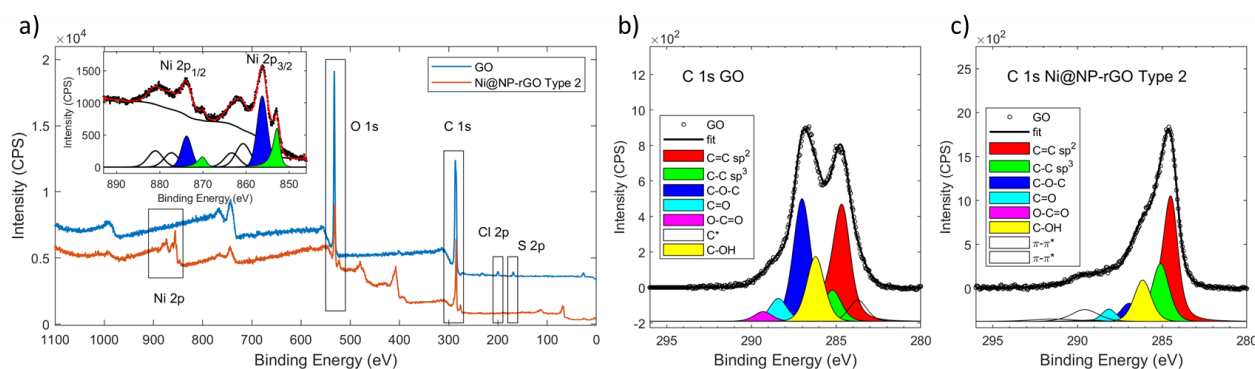
Figure 5. a) XPS survey spectra of GO and **NiNP@rGO Type 2**, inset Ni 2p signal fitted with two doublets after Shirley background subtraction: blue for Ni(II) and green for Ni(0), other high energy peaks are shake-up transition. b) C 1s signal of pristine GO and c) **NiNP@rGO Type 2**.
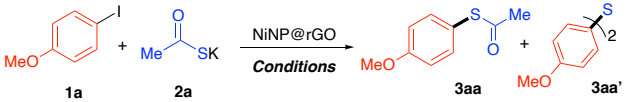
Applications of the NiNPs to the C-S forming cross-couplings

Firstly, we decided to test the reactivity of the obtained composites **NiNP@rGO Type 1** and **Type 2** in a model reaction comprising 4-iodoanisole **1a** and potassium thioacetate **2a** as model substrates. Interestingly, **NiNP@rGO Type 1** promoted the coupling (entry 1, Table 2) in 60% overall conversion (30% **3aa**) and poor chemoselectivity. As a matter of fact, the desired

thioacetate **3aa** and the aryl sulfide **3aa'** were obtained in a 2:1 ratio. Differently, the **NiNP@rGO Type 2** displayed higher efficiency, by delivering the desired aryl-thioacetate **3aa** in 60% yield, (**3aa:3aa'** > 25:1, entry 2).[18] These preliminary outcomes clearly highlight that, the smaller the metal-particle size and distribution average, the higher the catalytic performance. This aspect is frequently encountered in nanocatalyzed organic transformations.[19] Interestingly, the use of xylene as reaction medium at 150 °C proved superior with respect to other reaction

conditions screened (*i.e.* solvents as well as temperatures, entries 3-6), while a slight improvement in the isolated yield (72%) was recorded by increasing the **1a:2a** ratio up to 1:8 (**3aa:3aa'** > 25:1) and lowering the reaction concentration to 0.1 M. Interestingly, attempt to carry out the titled cross-coupling event under homogenous regime ((PPh₃)₂NiCl₂/Zn 10 mol%)[20] failed (entry 11) emphasizing the role of the carbon-based support in modulating the activity of the dispersed **NiNPs**. Finally, the blank reaction carried out with rGO proved the genuine metal catalysis of the present C-S bond forming protocol (entry 12).[21]

Table 2. Optimization of the reaction conditions of the C-S cross-coupling reaction.

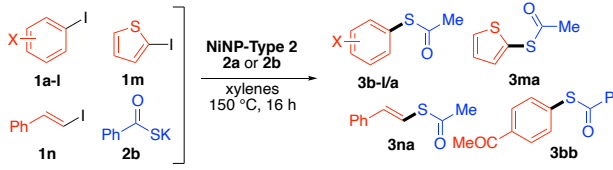| Run[a]	NiNP@rGO	Conditions	Yield (%) 3aa[b]	3:3'[c]
1	**Type 1**	xylene, 150 °C	30[d]	2:1
2	**Type 2**	xylene, 150 °C	60	> 25:1
3	**Type 2**	Toluene, 100 °C	traces	--
4	**Type 2**	DMF, 100 °C	traces	--
5	**Type 2**	mesitylene, 150 C°	50	7:1
6	**Type 2**	PhCl, 150 °C	42	7.3:1
7[e]	**Type 2**	xylene, 150 °C	70	> 25:1
8[f]	**Type 2**	xylene, 150 °C	72	> 25:1
10[g]	**Type 2**	xylene, 150 °C	59	> 25:1
11[h]	**[Ni]**	xylene, 150 °C	NR	--
12	**rGO**	xylene, 150 °C	NR	--

[a] All the reactions were carried out under nitrogen and degassed solvent for 16 h. **1a:2a** (1:6), [**1a**]: 0.2 M, NiNP@rGO (8 mg), unless otherwise specified. [b] Isolated yield after flash chromatography. [c] Determined by ¹H-NMR analysis. [d] 1H-NMR conversion. [e] **1a:2a** = 1:8, reaction time 6.5 h. [f] [**1a**]: 0.1 M, **1a:2a** = 1:8. g) [**1a**]: 0.05 M, **1a:2a** = 1:8. h) With (PPh₃)₂NiCl₂ (10 mol%) and Zn (10 mol%) as the catalyst. NR: no reaction.

Then, based on the optimal reaction conditions, the generality of the methodology in terms of functional group tolerance was ascertained by subjecting a range of diversely substituted aryl/vinyl-iodides (**1b-n**) with potassium thioacetate **2a** and potassium thiobenzoate **2b** and the resulting outcomes are listed in the Table 3.

Tolerance towards different electron-withdrawing substituents was assessed with substrates **1b-d**. In particular, keto- and CN-substituted iodides **1b,c** delivered the respective thioacetylation products **3b,c** in good yields (up to 79%, entries 1,2). Notably, the possibility of accommodating a bromine substituent (**3d**, entry 3) highlighted the selectivity of the protocol towards aryl iodides, allowing the possibility of further transition metal-based functionalization. To our delight, the introduction of electron-donating substituents, different from methoxy (**3e,f**), worked just as efficiently (entries 4,5). Analogously, protected iodophenols or iodoanilines **1g** and **1h**, presenting sensitive moieties such as aryl acetates and trifluoroacetamides, worked smoothly in the protocol (entries 6,7, yield up to 54%). Moreover, introduction of electron-

withdrawing or electron-donating substituents at the *ortho*-position of the aromatic ring (**1j-1l**) did not hamper the reactivity, showing a general high tolerance towards steric hindrance (yield up to 79%, entries 9-11).

**Table 3.** Scope of the reaction: aryl iodides **1**.

Entry[a]	X (**1**)/2	Yield (%) 3[b]
1	4-COMe (**1b**)/**2a**	79 (**3ba**)
2	4-CN (**1c**)/**2a**	42 (**3ca**)
3	4-Br (**1d**)/**2a**	40 (**3da**)
4	4-Me (**1e**)/**2a**	82 (**3ea**)
5	4-OBn (**1f**)/**2a**	57 (**3fa**)
6	4-OAc (**1g**)/**2a**	52 (**3ga**)
7	4-NHC(O)CF₃ (**1h**)/**2a**	54 (**3ha**)
8	3-Me (**1i**)/**2a**	41 (**3ia**)
9	2-OMe (**1j**)/**2a**	79 (**3ja**)
10	2-F (**1k**)/**2a**	57 (**3ka**)
11	2-CO₂Me (**1l**)/**2a**	56 (**3la**)
12	2-thienyl (**1m**)/**2a**	80 (**3ma**)
13	2-styryl (**1n**)/**2a**	49 (**3na**)[c]
14	4-COMe (**1b**)/**2b**	56 (**3bb**)

[a] All the reactions were carried out under nitrogen and degassed solvent. **1:2** (1:8), [**1**]: 0.1 M, **NiNP@rGO Type 2**. [b] Isolated yield after flash chromatography. [c] The isomer *E*-**3na** was isolated in stereospecific manner.

Furthermore, the synthetic versatility of the protocol was proved not to be limited to substituted benzene rings, as was assessed by successful coupling of a heteroaryl iodide (2-iodothiophene **1m**, entry 12), as well as a vinyl iodides (**1n**, entry 13) in synthetically good yields and stereospecific manner. Additionally, potassium thiobenzoate **2b** proved competent in the model reaction, delivering the cross-coupling product **3bb** in 56% yield under optimal conditions (entry 14).[22]

Mechanistically, a tentative pictorial sketch is presented in Scheme 2. The Ni(0) nanoparticles could initially undergo oxidative addition on the aryl-iodides **1**, providing the corresponding aryl-Ni(II) species **A**. Ligand metathesis with the thiocarboxylate salt **2** would generate the Ni(II)-thiocarboxylate **B** that could evolve into the desired aryl-thiocarboxylate **3** via reductive elimination. Although a conclusive answer about possible Ni(0)/Ni(II) or Ni(I)/Ni(III) redox-couple based mechanisms is still not available, the high temperatures required for the present cross-coupling protocol[23] and the morphological information gained by the XPS analysis, prompted us to exclude the involvement of Ni(I) and Ni(III) intermediates during the reaction course.
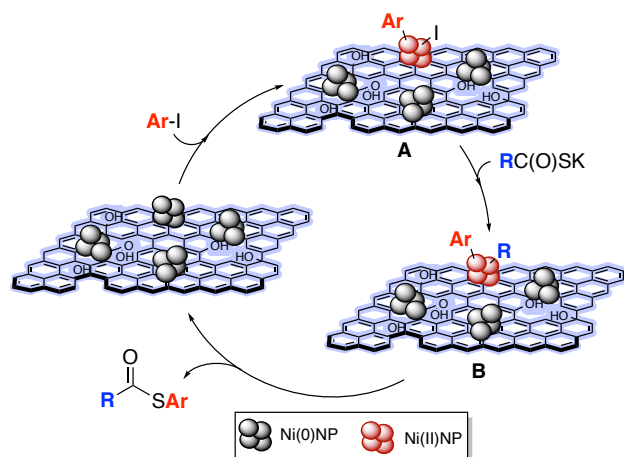
Scheme 2. Pictorial sketch of the proposed reaction mechanism.

Additionally, in order to get insights into the formation of the by-products **3'**, a dedicated experimental control was carried out. In particular, when **3aa** was reacted under optimal conditions (*i.e.* **NiNP@rGO**-**Type-2**, xylene, 150 °C), **3aa'** was formed in 50% conversion. This evidence proved the competence of aryl-thioacetates **3** in providing sulphide **3'** probably via **NiNP@rGO** assisted formation of thiophenols (i.e. deacetylation of **3**), followed by conversion cross-coupling pathway involving the aryl iodides.

To assess the genuine heterogenous catalysis, substrate **1b** was subjected to the optimized reaction conditions, stopping the reaction by filtering off the material when 30% conversion was reached. By re-heating the filtered reaction mixture at 150 °C for 15 h, no further conversion was observed. This suggests that no leaching of any active form of the catalyst from the material occurs during the reaction course. To support this experimental evidence, a model reaction was carried out and after complete consumption of the starting material, an XRD analysis was carried out on the dried mother liquors upon removal of the insoluble materials (see Supporting Information). Interestingly, no evidence of Ni-containing species was recorded. Moreover, no appreciable reactivity of the starting material (**1b**) or product (**3ba**) is occurring in the absence of the catalyst. Unfortunately, attempts to re-use the filtered **NiNP@rGO Type 2** in subsequent reactions led to unsatisfactory results and only moderate conversion was detected by re-adding fresh reagents upon completion of the first coupling. Interestingly, the XRD analysis of the recovered sold material revealed a significant morphological modification of the native **NiNP@rGO Type 2** composite and evidenced the presence of rather inactive Ni-S materials on the rGO support (see supporting information). This evidence is in contrast with a previously reported NiNP@rGO assisted thioarylation of iodoarenes in which reusability up to 6 times was documented. Although a conclusive answer to address this dichotomy is still not available, we could reason that the generation of thiocarboxylate by-products featuring a softer nature with respect to thiophenols could address for the amplified poisoning effect on the NiNP showed in our protocol.

Conclusions

In conclusion, with this study we synthetized two- types of Ni-nanocomposites based on nanoparticles dispersed on rGO. Full spectroscopic characterization revealed a marked dependence of the morphology and chemical nature of the nanostructures on the synthetic methodology. Analogously, a narrow structure/catalytic activity relationship was observed by testing the NiNPs in the thiocarboxylation cross-coupling between potassium thiocarboxylates and a range of diversely functionalized aryl/vinyl-iodides (yield up to 82%). Attempts to extend the present cross-coupling methodology to different Ni(0)-mediated processes are underway in our laboratories and will be presented in due course.

The experimental section has no title; please leave this line here.

^{1}H-NMR spectra were recorded on Varian 400 (400 MHz) spectrometers. Chemical shifts are reported in ppm from TMS with the solvent resonance as the internal standard (deuterochloroform: 7.24 ppm). Data are reported as follows: chemical shift, multiplicity (s = singlet, d = doublet, dd= doublet doublet, t = triplet, td = triple doublet, dt = double triplet, q = quartet, sext = sextet, sept = septet, p = pseudo, b = broad, m = multiplet), coupling constants (Hz). ^{13}C-NMR spectra were recorded on a Varian 400 (100 MHz) spectrometers with complete proton decoupling. Chemical shifts are reported in ppm from TMS with the solvent as the internal standard (deuterochloroform: 77.0 ppm).

GC-MS spectra were taken by EI ionization at 70 eV on a Hewlett-Packard 5971 with GC injection. They are reported as: *m/z* (rel. intense). LC-electrospray ionization mass spectra were obtained with Agilent Technologies MSD1100 single-quadrupole mass spectrometer. Chromatographic purification was done with 240-400 mesh silica gel. Anhydrous solvents were supplied by Sigma Aldrich in Sureseal® bottles and used without any further purification. Commercially available chemicals were purchased from Sigma Aldrich, Fluorochem and TCI and used without any further purification. GO and rGO (partly reduced, 85% atomic C) were purchased from Abalonyx. Agilent Technologies LC/MSD Trap 1100 series (nebulizer: 15.0 PSI, dry Gas: 5.0 L/min, dry Temperature: 325 °C, capillary voltage positive scan: 4000 mA, capillary voltage negative scan: 3500 mA). X-ray diffraction (XRD) patterns were collected in Bragg-Brentano geometry by means of a Malvern Panalytical MRD diffractometer equipped with a copper source (lambda = 0.15418 nm). Each step of 0.1° 2-theta was integrated for 100 s with a multi-channel solid state detector, in the range 5.0° - 90°.

Aryl iodides **1f**,[24a] **1g**,[24b] **1j**,[24c] were prepared from the corresponding phenols via known procedures. Aryl iodide **1h**[24d] was prepared from 4-iodoaniline according to a known procedure. Aryl iodide **1l**[24e] was prepared by esterification of the corresponding benzoic acid. Vinyl iodide **1n**[24f] was prepared from cinnamic acid according to a known procedure. All other iodides are commercially available.

Potassium thiobenzoate **2b** was prepared from benzoyl chloride in two steps: thioacid formation using NaHS[25a] and subsequent salification using KOH in MeOH.[25b]

Synthesis of *the NiNP@rGO*.

NiNP@rGO Type 1 The synthesis previously reported in the literature was adopted.[11a]

NiNP@rGO Type 2.[11e] A 250 mL round-bottom flask was charged with 100 mg of GO and 60 mL of ethylene glycol. The suspension was ultrasonicated for 2 h to disperse GO. Then, a solution of $NiCl_2 \cdot 6H_2O$ (570 mg) in 40 mL (3:1 H_2O:ethylene glycol) was added to the GO dispersion. The mixture was stirred at 50 °C for 2 h and then transferred into a flame dried 500 mL three-necked round bottom flask equipped with dropping funnel and condenser under nitrogen atmosphere. After degassing the mixture by bubbling nitrogen gas, a solution of $NaBH_4$ (302 mg) in 80 mL H_2O was

slowly added dropwise (CAUTION!! molecular hydrogen gas evolution will occur) and the mixture was subsequently heated to 110 °C and stirred for 2 h. The mixture was allowed to cool down and decanted overnight. The upper solution was removed by pipette, and the material was washed by centrifugation with water (3 x 75 mL) and then methanol (2 x 75 mL). The material was transferred to a glass vial and dried under vacuum to yield **NiNP@rGO Type 2 (170 mg)**.

Thiocarboxylation cross-coupling. A flame dried Schlenk tube was charged, under nitrogen, with reagent grade xylenes (mixture of isomers, 0.8 mL, degassed by nitrogen bubbling). Then, potassium thiocarboxylates **2** (0.8 mmol), rGO/Ni catalyst (8 mg) and iodide **1** (0.1 mmol), were added in a sequence. The reaction vessel was sealed, and the mixture was stirred at 150 °C for 18 h (see SI for details). The mixture was filtered on a cotton plug and the heterogeneous catalyst and inorganic compounds (potassium thiocarboxylate and KI) washed with Et$_2$O. The filtrate was evaporated at reduced pressure to remove the volatiles and then directly charged as xylene solution into column for flash chromatography purification.

3aa-*S*-(4-methoxyphenyl) ethanethioate. Colorless oil. *n*Hex:EtOAc: 10:1. Yield = 72%. **¹H NMR** (400 MHz, CDCl$_3$) δ = 7.35 – 7.29 (m, 2H), 6.97 – 6.91 (m, 2H), 3.83 (s, 3H), 2.39 (s, 3H); **¹³C NMR** (100 MHz, CDCl$_3$) δ = 195.3, 160.8, 136.2, 118.9, 115.0, 55.5, 30.1; **GC-MS**: *m/z* (%) = 182 (15), 140 (100), 125 (41); **Anal. Calc.** for (C$_9$H$_{10}$O$_2$S: 182.24): C, 59.32; H, 5.53; found: C, 59.35; H, 5.48.

3ba-*S*-(4-acetylphenyl) ethanethioate. Off-white solid (m.p. = 118-120 °C). *n*Hex:EtOAc: 5:1. Yield = 79%. **¹H NMR** (400 MHz, CDCl$_3$) δ = 8.01 – 7.95 (m, 2H), 7.56 – 7.48 (m, 2H), 2.61 (s, 3H), 2.46 (s, 3H); **¹³C NMR** (100 MHz, CDCl$_3$) δ = 197.4, 192.8, 137.5, 134.3, 133.9, 128.9, 30.6, 26.8; **GC-MS**: *m/z* (%) = 194 (10), 152 (100), 137 (87), 108 (41); **Anal. Calc.** for (C$_{10}$H$_{10}$O$_2$S: 194.25): C, 61.83; H, 5.19; found: C, 62.01; H, 5.01.

3ca-*S*-(4-cyanophenyl) ethanethioate. Yellow solid (m.p. = 95-96 °C). *n*Hex:EtOAc: 7:1. Yield = 42%. **¹H NMR** (400 MHz, CDCl$_3$) δ = 7.68 (d, *J* = 8.4 Hz, 2H), 7.55 – 7.51 (m, 2H), 2.47 (s, 3H); **¹³C NMR** (100 MHz, CDCl$_3$) δ = 192.0, 134.8, 134.5, 132.8, 118.4, 113.3, 30.8; **GC-MS**: *m/z* (%) = 177 (40), 135 (96), 134 (100), 107 (51); **Anal. Calc.** for (C$_9$H$_7$NOS: 177.22): C, 61.00; H, 3.98; found: C, 61.09; H, 4.07.

3da-*S*-(4-bromophenyl) ethanethioate. Colorless crystalline plates (m.p. = 99-101 °C). *n*Hex:EtOAc: 15:1. Yield = 40%. **¹H NMR** (400 MHz, CDCl$_3$) δ = 7.56 – 7.52 (m, 2H), 7.29 – 7.26 (m, 2H), 2.43 (s, 3H); **¹³C NMR** (100 MHz, CDCl$_3$) δ = 193.4, 136.0, 132.6, 127.1, 124.3, 30.4; **GC-MS**: *m/z* (%) = 232 (⁸¹Br, 21), 230 (⁷⁹Br, 21), 190 (⁸¹Br, 85) 188 (⁷⁹Br, 85), 108 (100); **Anal. Calc.** for (C$_8$H$_7$BrOS: 231.11): C, 41.58; H, 3.05; found: C, 41.69; H, 3.03.

3ea-*S*-(*p*-tolyl) ethanethioate. Colorless oil. *n*Hex:EtOAc: 20:1. Yield = 82%. **¹H NMR** (400 MHz, CDCl$_3$) δ = 7.32 – 7.28 (m, 2H), 7.24 – 7.20 (m, 2H), 2.41 (s, 3H), 2.38 (s, 3H); **¹³C NMR** (100 MHz, CDCl$_3$) δ = 194.8, 139.9, 134.6, 130.2, 124.6, 30.2, 21.5; **GC-MS**: *m/z* (%) = 166 (15), 124 (100), 91 (77); **Anal. Calc.** for (C$_9$H$_{10}$OS: 166.24): C, 65.03; H, 6.06; found: C, 64.99; H, 6.11.

3fa-*S*-(4-(benzyloxy)phenyl) ethanethioate. White powder (m.p. = 105-107 °C). *n*Hex:EtOAc: 15:1. Yield = 57%. **¹H NMR** (400 MHz, CDCl$_3$) δ = 7.47 – 7.37 (m, 4H), 7.37 – 7.30 (m, 3H), 7.05 – 6.99 (m, 2H), 5.08 (s, 2H), 2.40 (s, 3H); **¹³C NMR** (100 MHz, CDCl$_3$) δ = 195.2, 160.0, 136.6, 136.2, 128.8, 128.3, 127.6, 119.2, 115.9, 70.2, 30.1; **GC-MS**: *m/z* (%) = 258 (6), 216 (24), 91 (100); **Anal. Calc.** for (C$_{15}$H$_{14}$O$_2$S: 258.34): C, 69.74; H, 5.46; found: C, 69.81; H, 5.45.

3ga-4-(acetylthio)phenyl acetate. Off-white solid (m.p. = 106-108 °C). *n*Hex:EtOAc: 3:1. Yield = 52%. **¹H NMR** (400 MHz, CDCl$_3$) δ = 7.45 – 7.37 (m, 2H), 7.19 – 7.11 (m, 2H), 2.42 (s, 3H), 2.31 (s, 3H); **¹³C NMR** (100 MHz, CDCl$_3$) δ = 193.9, 169.2, 151.7, 135.7, 125.3, 122.6, 30.3, 21.3; **GC-MS**: *m/z* (%) = 210 (9), 168 (41), 126 (100); **Anal. Calc.** for (C$_{10}$H$_{10}$O$_3$S: 210.25): C, 57.13; H, 4.79; found: C, 69.81; H, 5.45.

3ha-*S*-(4-(2,2,2-trifluoroacetamido)phenyl) ethanethioate. Off-white solid (m.p. = 174-177 °C). *n*Hex:EtOAc: 4:1. Yield = 54%. **¹H NMR** (400 MHz, CDCl$_3$) δ = 8.18 (bs, 1H), 7.64 – 7.55 (m, 2H), 7.43 – 7.33 (m, 2H), 2.45

(s, 3H); **¹³C NMR** (100 MHz, CDCl$_3$) δ = 194.8, 154.9 (q, *J* = 37.7 Hz), 136.6, 135.7, 125.3, 121.1, 115.7 (q, *J* = 288.7 Hz), 30.3; **¹⁹F NMR** (376 MHz, CDCl$_3$) δ = -75.73 (s, 3F); **GC-MS**: *m/z* (%) = 263 (32), 221 (100), 152 (32); **Anal. Calc.** for (C$_{10}$H$_8$F$_3$O$_2$S: 263.33): C, 45.63; H, 3.06; found: C, 45.69; H, 2.97.

3ia-*S*-(*m*-tolyl) ethanethioate. Colorless oil. *n*Hex:EtOAc: 20:1. Yield = 41%. **¹H NMR** (400 MHz, CDCl$_3$) δ = 7.33 – 7.28 (m, 1H), 7.25 – 7.20 (m, 3H), 2.41 (s, 3H), 2.37 (s, 3H); **¹³C NMR** (100 MHz, CDCl$_3$) δ = 194.5, 139.2, 135.2, 131.7, 130.5, 129.2, 127.7, 30.3, 21.4; **GC-MS**: *m/z* (%) = 166 (18), 124 (100), 91 (73); **Anal. Calc.** for (C$_9$H$_{10}$OS: 166.24): C, 65.03; H, 6.06; found: C, 65.11; H, 5.97.

3ja-*S*-(2-methoxyphenyl) ethanethioate. Viscous oil. *n*Hex:EtOAc: 9:1. Yield = 79%. **¹H NMR** (400 MHz, CDCl$_3$) δ = 7.45 – 7.37 (m, 2H), 7.05 – 6.93 (m, 2H), 3.86 (s, 3H), 2.41 (s, 3H); **¹³C NMR** (100 MHz, CDCl$_3$) δ = 193.7, 159.3, 136.9, 131.9, 121.3, 116.3, 111.7, 56.1, 30.2 **GC-MS**: *m/z* (%) = 182 (10), 140 (100), 125 (36); **Anal. Calc.** for (C$_9$H$_{10}$O2S: 182.24): C, 59.32; H, 5.53; found: C, 59.41; H, 5.55.

3ka-*S*-(2-fluorophenyl) ethanethioate. Colorless oil. *n*Hex:EtOAc: 20:1. Yield = 57%. **¹H NMR** (400 MHz, CDCl$_3$) δ = 7.50 – 7.37 (m, 2H), 7.25 – 7.13 (m, 2H), 2.45 (s, 3H); **¹³C NMR** (100 MHz, CDCl$_3$) δ = ¹³C NMR (101 MHz, cdcl$_3$) δ 192.2, 162.2 (d, *J* = 249.5 Hz), 136.8 (d, *J* = 0.8 Hz),132.3 (d, *J* = 8.2 Hz), 124.8 (d, *J* = 3.9 Hz), 116.4 (d, *J* = 22.7 Hz), 115.5 (d, *J* = 18.6 Hz), 30.2; **¹⁹F NMR** (376 MHz, CDCl$_3$) δ = -106.74 (dt, *J* = 8.5, 6.3 Hz, 1F); **GC-MS**: *m/z* (%) = 170 (16), 128 (100); **Anal. Calc.** for (C$_8$H$_7$FOS: 170.20): C, 56.46; H, 4.15; found: C, 56.38; H, 4.20.

3la-methyl 2-(acetylthio)benzoate. Pale yellow oil. *n*Hex:EtOAc: 6:1. Yield = 56%. **¹H NMR** (400 MHz, CDCl$_3$) δ = 7.93 (dd, *J* = 7.5, 1.2 Hz, 1H), 7.58 – 7.55 (m, 1H), 7.53 (td, *J* = 7.4, 1.5 Hz, 1H), 7.46 (td, *J* = 7.6, 1.7 Hz, 1H), 3.89 (s, 3H), 2.43 (s, 3H); **¹³C NMR** (100 MHz, CDCl$_3$) δ = 193.2, 166.8, 136.7, 134.0, 132.0, 131.0, 129.4, 128.8, 52.5, 30.4; **GC-MS**: *m/z* (%) = 210 (5), 168 (56), 136 (100); **Anal. Calc.** for (C$_{10}$H$_{10}$O$_3$S: 210.04): C, 57.13; H, 4.79; found: C, 57.02; H, 4.79.

3ma-*S*-(thiophen-2-yl) ethanethioate. Colourless oil. *n*Hex:EtOAc: 20:1. Yield = 80%. **¹H NMR** (400 MHz, CDCl$_3$) δ = 7.56 (dd, *J* = 5.3, 1.2 Hz, 1H), 7.17 (dd, *J* = 3.6, 1.2 Hz, 1H), 7.11 (dd, *J* = 5.3, 3.6 Hz, 1H), 2.41 (s, 3H); **¹³C NMR** (100 MHz, CDCl$_3$) δ = 194.4, 135.9, 132.0, 128.0, 125.2, 29.6; **GC-MS**: *m/z* (%) = 158 (27), 116 (100), 71 (77); **Anal. Calc.** for (C$_6$H$_6$OS$_2$: 158.23): C, 45.54; H, 3.82; found: C, 45.55; H, 3.69.

3na-(*E*)-*S*-styryl ethanethioate. Viscous oil. *n*Hex:EtOAc: 30:1. Yield = 49%. **¹H NMR** (400 MHz, CDCl$_3$) δ = 7.43 – 7.37 (m, 2H), 7.36 – 7.30 (m, 2H), 7.29 – 7.24 (m, 1H), 7.23 (d, *J* = 16.3 Hz, 1H), 6.72 (d, *J* = 16.3 Hz, 1H), 2.41 (s, 3H); **¹³C NMR** (100 MHz, CDCl$_3$) δ = 192.8, 136.2, 131.8, 128.8, 128.3, 126.5, 117.3, 30.7; **GC-MS**: *m/z* (%) = 178 (18), 136 (100), 91 (76); **Anal. Calc.** for (C$_{10}$H$_{10}$OS: 178.25): C, 67.38; H, 5.66; found: C, 67.33; H, 5.60.

3bb-*S*-(4-acetylphenyl) benzothioate. White solid (m.p. = 123-126 °C). *n*Hex:EtOAc: 6:1. Yield = 56%. **¹H NMR** (400 MHz, CDCl$_3$) δ = 8.06 – 7.99 (m, 4H), 7.67 – 7.59 (m, 3H), 7.55 – 7.46 (m, 2H), 2.64 (s, 3H). **¹³C NMR** (100 MHz, CDCl$_3$) δ = 197.4, 189.0, 137.5, 136.3, 134.9, 134.0, 133.4, 128.9, 128.8, 127.5, 26.7; **GC-MS**: *m/z* (%) = 256 (5), 105 (100), 77 (63); **Anal. Calc.** for (C$_{15}$H$_{12}$O$_2$S: 256.06): C, 70.29; H, 4.72; found: C, 70.33; H, 4.66.

funding of the project #18668 "Tecnologie avanzate per il controllo e lo sviluppo di molecole innovative per la salute".

Supporting Information

Yes

Conflict of Interest

The authors declare no conflict of interest.

References

(1) For general reviews see: Johansson Seechurn, C. C. C.; Kitching, M. O.; Colacot, T. J.; Snieckus, V. *Angew. Chem. Int. Ed.* **2012**, *51*, 5062.

(2) (a) Tasker, S. Z.; Standley, E. A.; Jamison, T. F. *Nature* **2014**, *509*, 299. (b) Hazari, N.; Melvin, P. R.; Beromi, M. M. *Nat. Rev. Chem.* **2017**, *1*, 0025. (c) Yaqiong, L.; Yuhang, F.; Qianfa, J. *Chin. J. Org. Chem.* **2019**, *39*, 350. (d) Nebra, N. *Molecules*, **2020**, *25*, 1141. (e) Zhu, C.; Yue, H.; Jia, J.; Rueping, M. *Angew. Chem. Int. Ed.* **2021**, *60*, 17810.

(3) (a) Liu, L.; Corma, A. *Chem. Rev.* **2018**, *118*, 4981. (b) Ndoloming, M. J.; Bingwa, N.; Meijboom, R. *J. Mater. Sci.* **2020**, *55*, 6195. (c) Jaji, N.-D.; Lee, H. L.; Hussin, M. H.; Akil, H. M.; Zakaria, M..; Hafi Othman, M. B. *Nanotech. Rev.* **2020**, *9*, 1456.

(4) For a collection of representative examples see: (a) Bhowmik, K.; Sengupta, D.; Basu, B., De, G. *RSC Adv.* **2014**, *4*, 35442. (b) Hussain, N.; Gogoi, P.; Khare, P.; Das, M.R. *RSC Adv.* **2015**, *5*, 103105. (c) Keyhaniyan, M.; Shiri, A.; Eshighi, H.; Khojastehnezhad, A. *New J. Chem.* **2018**, *42*, 19433. (c) Bathla, A.; Patil, B. *ChemistrySelect* **2018**, *3*, 4738. (d) Dong, Y.; Jv, J.-J.; Li, Y.; Li, W.-H.; Chen, Y.-Q.; Sun, Q.; Ma, J.-P.; Dong, Y.-B. *RSC Adv.* **2019**, *9*, 20266. (e) Adam, A. A.; Szabados, M.; Polyakovics, A.; Konya, Z.; Kukovecz, A.; Sipos, P.; Palinko, I. *J. Nanosci. Nanotechnol.* **2019**, *19*, 453. (f) Li, Y.; Hu, Y.; Shi, F.; Li, H.; Xie, W.; Chen, J. *Angew. Chem. Int. Ed.* **2019**, *58*, 9049. (g) Naeimi, H.; Kiani, F. *J. Organomet. Chem.* **2019**, *885*, 65. (h) Nan, L.; Yalan, C.; Jixiang, L.; Dujuan, O.; Wenhui, D.; Rouhi, J.; Mustapha, M. *RSC Adv.* **2020**, *10*, 27923. (g) Adam, A. A.; Szabados, M.; Varga, G.; Papp, A.; Musza, K.; Konya, Z.; Kukovecz, A.; Sipos, P.; Palinko, I. *Nanomaterial,* **2020**, *10*, 632. (i) Raoufi, F.; Manojjemi, M.; Aghaei, H.; Zare, K.; Ghaedi, M. *ChemistrySelect* **2020**, *5*, 211. (l) Murugan, K.; Nainamalai, D.; Kanagaraj, P.; Nagappan, S.G.; Palaniswamy, S. *Appl. Organomet. Chem.* **2020**, *34*, e5778; (m) Keyhaniyan, M.; Khojastehnezhad, A.; Eshighi, H.; Shiri, A. *Appl. Organomet. Chem.* **2021**, *35*:e6158. (n) Bhakta, S.; Ghosh, T. *ChemCatChem*, **2021**, *13*, 828, and references therein.

(5) Łastawiecka, E.; Flis, A.; Stankevič, M.; Greluk, M.; Słowikb, G.; Gac, W. *Org. Chem. Front.* **2018**, *5*, 2079.

(6) (a) M. Platon, N. Wijaya, V. Rampazzi, L. Cui, Y. Rousselin, M. Saeys, J.-C. Hierse, *Chem. Eur. J.* **2014**, *20*, 12584-12594; (b) Sengupta, D.; Bhowmik, K.; De, G.; Basu, B. *Beilstein J. Org. Chem.* **2017**, *13*, 1796.

(7) Wang, N.; Saidhreddy, P.; Jiang, X. *Nat. Prod. Rep.* **2020**, *37*, 246.

(8) (a) Lee, C.-F.; Liu, Y.-C.; Badsara, S. S. *Chem. Asian J.* **2014**, *9*, 706, and references therein. (b) Taherinia, Z.; Ghorbani-Choghamarani, A. *Can. J. Chem.* **2019**, *97*, 46. (c) Panigrahi, R.; Sahu, S. K.; Behera, P. K.; Panda, S.; Rout, L. *Chem. Eur. J.* **2020**, *26*, 620. (d) Panda, S.; Sahu, S. K.; Behera, P. K.; Panigrahi, R.; Garnaik, B.; Rout, L. *New J. Chem.* **2020**, *44*, 2500. (e) Annamalai, P.; Liu, K.-C.; Badsara, S. S.; Lee, C.-F. *Chem. Rec.* **2021**, https://doi.org/10.1002/tcr.202100133. For electrochemical tools in oxidative C-S cross-coupling reaction see: Song, C.; Liu, K.; Dong, X.; Chiang, C.-W. *Synlett* **2019**, *30*, 1149.

(9) (a) Favaretto, L.; An, J.; Sambo, M.; De Nisi, A.; Bettini, C.; Melucci, M.; Kovtun, A.; Liscio, A.; Palermo, V.; Bottoni, A.; Zerbetto, F.; Calvaresi, M.; Bandini, M. *Org. Lett.* **2018**, *20*, 3705. (b) Lombardi, L.; Bellini, D.; Bottoni, A.; Calvaresi, M.; Monari, M.; Kovtun, A.; Palermo, V.; Melucci, M.; Bandini, M. *Chem. Eur. J.* **2020**, *26*, 10427

(10) (a) Ji, Z.; Shen, X.; Zhu, G.; Zhou, H.; Yuan, Z. *J. Mater. Chem.* **2012**, *22*, 3471. (b) Nabid, M. R.; Bide, Y.; Dastar, F. *Cat. Lett.* **2015**, *145*, 1798. (c) Liu, Y.; Gao, C.; Li, Q.; Pang, H. *Chem. Eur. J.* **2019**, *25*, 2141. (d) Al-Nafiey, A.; Al-Mamoori, M. H. K.; Alshrefi, S. M.; Shakir, A. K.; Ahmed, R. T. *Mat. Today: Proc.* **2019**, *19*, 94. (e) Zhang, X.; Chen, K.-H.; Zhou, Z.-H.; He, L.-H. *ChemCatChem* **2020**, *12*, 4825.

(11) Parodi, A.; Battaglioli, S.; Liu, Y.; Monari, M.; Marín-Luna, M.; Silva López, C.; Bandini, M. *Chem.Commun*, **2019**, *55*, 9669.

(12) Peng, K.; Gao, M.-Y., Yi, Y.-Y., Guo, J., Dong, Z.-B. *Eur. J. Org. Chem.* **2020**, *2020*, 1665. (b) Sundaravelu, N.; Sangeetha, S.; Sekar, G. *Org. Biomol. Chem.* **2021**, *19*, 1459.

(13) For examples of homogenous metal catalyzed thiocarboxylation reaction see: (a) Lai, C.; Backes, B. J. *Tetrahedron Lett.* **2007**, *48*, 3033. (b) van den Hoogenband, A.; Lange, J. H. M.; Broger, R. P. J.; Stoit, A. R.; Terpstra, J. W. *Tetrahedron Lett.* **2010**, *51*, 6877. (c) Park, N.; Park, K.; Jang, M.; Lee, S. *J. Org. Chem.* **2011**, *76*, 4371. (d) Sonica-Castro, S. M.; Peñéñory, A. B. *Beilstein J. Org. Chem.* **2013**, *9*, 467. (e) Soria-Castro, S. M.; Andrada, D. A.; Caminos, D. A.; Argüello, J. E.; Robert, M.; Peñéñory, A. B. *J. Org. Chem.* **2017**, *82*, 11464. (f) Olivito, F.; Costanzo, P.; Di Gioia, M. L.; Nardi, M.; Oliverio, M.; Procopio, A. *Org. Biomol. Chem.* **2018**, *16*, 7753.

(14) (a) Mazzaro, R.; Boni, A.; Valenti, G.; Marcaccio, M.; Paolucci, F.; Ortolani, L.; Morandi, V.; Ceroni, P.; Bergamini, G. *ChemistryOpen*, **2015**, *4*, 268. (b) Mazzaro, R.; Boni, A.; Valenti, G.; Marcaccio, M.; Paolucci, F.; Ortolani, L.; Morandi, V.; Ceroni, P.; Bergamini, G. *ChemistryOpen*, **2014**, *4*, 268.

(15) Kim, K. S.; Winograd, N. *Surf. Sci* **1974**, *43*, 625.

(16) Zhang, Z.; Matsubayashi, Z.; Grisafe, A.; Lee, B.; Lloyd, J. R. *Mat. Chem. Phys.* **2016**, *170*, 175.

(17) Kovtun, A.; Jones, D.; dell'Elce, S.; Treossi, E.; Liscio, A.; Palermo, V. *Carbon* **2019**, *143*, 268.

(18) See supporting information for a complete list of reaction condition screening

(19) Nasrallah, H. O.; Min, Y.; Lerayer, E.; Nguyen, T.-A.; Poinsot, D.; Roger, J.; Brandés, S.; Heintz, O.; Roblin, P.; Jolibois, F.; Poteau, R.; Coppel, Y.; Kahn, M.L.; Gerber, I.C.; Axet, M.R.; Serp, P.; Hierso, J.-C. *J. Am. Chem. Soc. Au* **2021**, *1*, 187-200..

(20) Sweeney, J. B.; Ball, A. K.; Smith, L. J. *Chem. Eur. J.* **2018**, *24*, 7354.

(21) Optimal reaction conditions involving **NiNP-Type 2** required ca. 25 mol% of Ni loading with respect to **1**.

(22) The present catalytic protocol displayed marked counterion dependance. As a matter of fact, sodium and cesium thioacetates proved inefficiency in the coupling protocol.

(23) Sun, R.; Qin, Y.; Nocera, D.G. *Angew. Chem. Int. Ed.* **2020**, *59*, 9527.

(24) (a) Uchiyama, M.; Furuyama, T.; Kobayashi, M.; Matsumoto, Y.; Tanaka, K. *J. Am. Chem. Soc.* **2006**, *128*, 8404. (b) Bull, S. R.; Palmer, L. C.; Fry, N. J.; Greenfield, M. A.; Messmore, B. W.; Meade, T. J.; Stupp, S. I. *J. Am. Chem. Soc.* **2008**, *130*, 2742. (c) Lee, K.; Ban, H. S.; Naik, R.; Hong, Y. S.; Son, S.; Kim, B.-K.; Xia, Y.; Song, K. B.; Lee, H.-S.; Won, M. *Angew. Chem. Int. Ed.* **2013**, *52*, 10286. (d) Melissaris, A. P.; Litt, M. H. *J. Org. Chem.* **1994**, *59*, 5818. e) Soltani, Y.; Wilkins, L. C.; Melen, R. L. *Angew. Chem. Int. Ed.* **2017**, *56*, 11995. (f) Xu, R.-S.; Yue, L.; Pan, Y.-J. *Tetrahedron* **2012**, *68*, 5046

(25) (a) Liu, H.; Zhao, L.; Yuan, Y.; Xu, Z.; Chen, K.; Qiu, S.; Tan, H. *ACS Catal.* **2016**, *6*, 1732. (b) Jixian, P.; Hui, W.; Zhongdong, S. CN 107840815 A, March 27, 2018. (Add 370 mL of methanol to a 1000 mL four-necked flask. Add 370 mL of ethanol and 51.4 g of thiobenzoic acid. Add 19.0 g of potassium hydroxide. The reaction was vigorously stirred at 50 °C for 2.5 hours. Concentrate the reaction to a yellow solid. Wash with 200 mL of diethyl ether. 59.4 g of potassium thiobenzoate was filtered, Yield 99%).